Thermal Properties of the Hot Core Population in Sagittarius B2 Deep South

Desmond Jeff,^{1,2} Adam Ginsburg,¹ Alyssa Bulatek,¹ Nazar Budaiev,¹ Álvaro Sánchez-Monge,^{3,4} Mélisse Bonfand,⁵ Cara Battersby,⁶ Fanyi Meng,⁷ Peter Schilke,⁸ and Anika Schmiedeke⁹

¹Department of Astronomy, University of Florida
211 Bryant Space Science Center P.O Box 112055 Gainesville, FL 32611-2055 USA

²National Radio Astronomy Observatory, 520 Edgemont Road, Charlottesville, VA 22903-2475, USA

³Institut de Ciències de l'Espai (ICE, CSIC), Carrer de Can Magrans s/n, E-08193, Bellaterra, Barcelona, Spain

⁴Institut d'Estudis Espacials de Catalunya (IEEC), Barcelona, Spain

⁵Departments of Astronomy & Chemistry, University of Virginia, Charlottesville, VA 22904, USA

⁶University of Connecticut, Department of Physics

196A Auditorium Road Unit 3046 Storrs, CT 06269 USA

⁷University of Chinese Academy of Sciences, Beijing 100049, China

⁸I. Physikalisches Institut, Universität zu Köln

Zülpicher Str. 77, 50937 Köln, Germany

⁹Green Bank Observatory, 155 Observatory Rd P.O. Box 2. Green Bank, WV 24944, USA

Submitted to ApJ

ABSTRACT

We report the discovery of 9 new hot molecular cores in the Deep South (DS) region of Sagittarius B2 using Atacama Large Millimeter/submillimeter Array Band 6 observations. We measure the rotational temperature of CH₃OH and derive the physical conditions present within these cores and the hot core Sgr B2(S). The cores show heterogeneous temperature structure, with peak temperatures between 252 and 662 K. We find that the cores span a range of masses (203-4842 M_{\odot}) and radii (3587-9436 AU). CH₃OH abundances consistently increase with temperature across the sample. Our measurements show the DS hot cores are structurally similar to Galactic Disk hot cores, with radii and temperature gradients that are comparable to sources in the Disk. They also show shallower density gradients than Disk hot cores, which may arise from the Central Molecular Zone's higher density threshold for star formation. The hot cores have properties which are consistent with those of Sgr B2(N), with 3 associated with Class II CH₃OH masers and one associated with an UCHII region. Our sample nearly doubles the high-mass star forming gas mass near Sgr B2(S) and suggest the region may be a younger, comparably massive counterpart to Sgr B2(N) and (M). The relationship between peak CH₃OH abundance and rotational temperature traced by our sample and a selection of comparable hot cores is qualitatively consistent with predictions from

Corresponding author: Desmond Jeff

d.jeff@ufl.edu

chemical modeling. However, we observe constant peak abundances at higher temperatures ($T \gtrsim 250$ K), which may indicate mechanisms for methanol survival that are not yet accounted for in models.

1. INTRODUCTION

The Central Molecular Zone (CMZ) is the closest "extreme" environment in which we can resolve individual sites of star formation. It is characterized by high molecular gas densities $(\sim 10^4 \text{ cm}^{-3}, \text{ Lis & Carlstrom (1994); Mills})$ et al. (2018)) and enrichment with complex molecules (Belloche et al. 2013). This environment is analogous to environments that were present near the peak in the cosmic star formation rate ($z \sim 2$, Kruijssen & Longmore (2013)), providing a vital laboratory within which to investigate how star formation proceeded during that era and in current sites of vigorous star formation (e.g., LIRGs and ULIRGs, Armus et al. (2009)). Massive stars are a crucial component in these investigations, given the role they play in injecting various kinds of feedback into the interstellar medium of their host galaxies (e.g., Meurer et al. (1995); Zinnecker & Yorke (2007); Ramachandran et al. (2018)). However, owing to their distance and brevity of their lifetimes, the earliest phases of massive stellar evolution are difficult to observe (e.g., Zinnecker & Yorke (2007); Battersby et al. (2017); Motte et al. (2018)). Massive protostars reach the main sequence while still heavily embedded in their natal envelopes, preventing direct observation of the earliest phases of their formation processes. Instead, we can study the composition and physical conditions within the protostellar envelope to infer the characteristics of the embedded protostar.

Located ~ 100 pc in projection away from Sgr A*, the CMZ molecular cloud Sagittarius B2 (Sgr B2) is the most massive ($\sim 10^7 {\rm M}_{\odot}$) molecular cloud in the galaxy (Lis & Goldsmith 1990). It shows a high degree of chemical enrichment, with many molecules being detected first in Sgr B2 (McGuire 2018) and many

more continuing to be found (Belloche 2018). It has also been described as undergoing a "ministarburst" event, containing > 70 high-mass stars, Class II methanol (CH₃OH) masers, water (H₂O) masers, diffuse and ultra-compact HII (UCHII) regions, and > 200 3 mm compact continuum sources that have been identified as YSOs (e.g., Ginsburg et al. (2018), Budaiev et al. (2024)). Several of these 3 mm continuum sources have been further identified as hot molecular cores (Bonfand et al. 2017; Sánchez-Monge et al. 2017), which are sites of highmass star formation that show emission from rare and complex molecular species (Cesaroni 2005). These sources are thought to represent a key phase in massive protostellar evolution and the chemical evolution of the ISM, as the antecedents to UCHII regions and formation sites of complex organic molecules (COMs, Herbst & van Dishoeck (2009)). The presence of hot cores in Sgr B2 thus makes it an ideal region within which to observe ongoing high-mass star formation and its influence on the physical and chemical properties of the surrounding gas.

Sgr B2 can be subdivided into four main regions: the protocluster complexes, B2(N)orth, (M)ain, and (S)outh; and the molecular ridge, Deep South (DS) (Schmiedeke et al. 2016). Prior studies in this region have primarily focused on Sgr B2(N) and (M) due to their relative brightness, chemical enrichment, and numerous sites of active high mass star formation. This has left Sgr B2(S) and (DS) relatively unexplored until recently, with the discovery of an arc of YSOs and non-thermal radio emission in (DS) (Ginsburg et al. 2018; Meng et al. 2019). Given that (DS) only contains one known HII region in Sgr B2(S) (Lu et al. 2019; Meng et al. 2022) and numerous embedded YSOs, it is thought that it is in an earlier phase of star formation than its counterparts in (N) and (M). It therefore represents a unique opportunity to observe the early phases of high mass star formation in the CMZ.

CH₃OH is a molecule of particular interest in star formation studies. It is the simplest COM and is believed to be one of several "parent" molecules necessary for the formation of more complex COMs (Nomura & Millar 2004; Garrod & Herbst 2006; Taquet et al. 2016). The abundances of COMs are often measured against the abundance of CH₃OH when testing the effects of physical conditions on COM formation rates (Requena-Torres et al. 2008; Herbst & van Dishoeck 2009; Bonfand et al. 2019). However, in spite of its utility and importance in star formation and astrochemical studies, the conditions leading to CH₃OH formation at the observed abundances remain under investigation (Sánchez-Monge et al. 2017; Bonfand et al. 2019). This is especially true in the CMZ.

In this paper, we report the discovery and the CH₃OH-derived physical characteristics of 9 hot molecular cores through the Deep South (DS) region of Sgr B2. In Section 2, we describe our data-reduction and analysis procedure. In Section 3, we discuss the spectral characteristics of the hot cores and their thermochemical properties. In Section 4, we discuss the biases that may affect our CH₃OH temperature and abundance measurements, physical mechanisms which may be responsible for our measurements, and compare the hot cores of Sgr B2(DS) to a selection of Galactic Disk hot cores and neighboring hot cores in Sgr B2(N). We summarize our conclusions in Section 5.

2. METHODS

2.1. Data reduction and imaging

We have carried out this work using 12 m Band 6 data collected as a part of ALMA Project Code 2017.1.00114.S (PI: Ginsburg). The full dataset consists of 10 fields that cover

the arc of 3 mm continuum sources identified in Ginsburg et al. (2018), as shown in Figure 1.

Each field contains four spectral windows, centered on 217.35, 219.20, 231.30, and 233.18 GHz, respectively. Each spectral window has a bandwidth of 1.875 GHz and a spectral resolution of 488 kHz (~ 0.6 km s⁻¹). Data cubes for each spectral window were produced using a robust parameter of 0 and by cleaning to a threshold of 3σ above the noise (3.09 mJy) using tclean (CASA version 5.6.0, McMullin et al. (2007)).

Due to the density of emission lines in chemically rich sources like hot cores, identifying line-free channels for continuum subtraction is challenging. After identifying sources (See Section 2.2.1), we use the --continuum mode of STAT-CONT (Sánchez-Monge et al. 2018) to perform continuum subtraction on each spectral window. This allows us to identify the hot core's continuum level and associated standard deviation (σ) in each pixel.

We produced a continuum image by combining all four spectral windows with tclean. It was cleaned to a threshold of 1 mJy and imaged with a Briggs robust parameter of 2, achieving a beam size of $0.36'' \times 0.29''$. The largest angular scale (LAS) of our observations was 2.075'', and our pixel scale was 0.05''. To account for filtering of large-scale continuum emission, we use uvcombine to feather the Atacama Large Millimeter/submillimeter Array (ALMA) observations with 1.1 mm continuum data from the Bolocam Galactic Plane Survey (Ginsburg et al. 2013). The LAS in their work is $\sim 2'$. The lowest noise level away from bright sources in the feathered continuum image is ~ 0.2 mJy.

2.2. Data Analysis

2.2.1. Source Identification

To identify hot core candidates, we begin by performing a by-eye examination of the 1 mm molecular line cubes. Canonical hot cores are

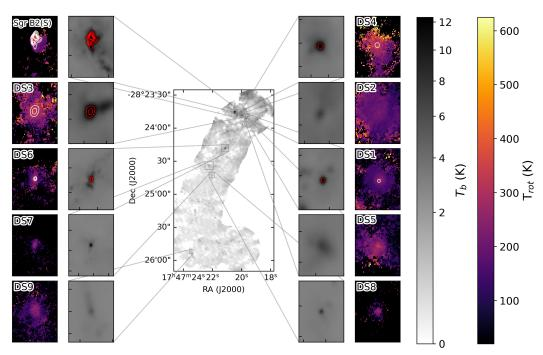


Figure 1. 1 mm dust continuum of Sgr B2(DS) after feathering with Bolocam Galactic Survey data of Sgr B2 (Ginsburg et al. 2013). The inset images show the CH_3OH temperature maps from each hot core (outer) and its corresponding continuum emission (inner). Red contours indicate regions where the continuum brightness exceeds 12 K (levels are at 12, 18, 24, 30, and 36 K).

compact sources, with radii $\lesssim 0.1$ pc (e.g., (Cesaroni 2005)). We therefore define candidate hot cores as sources that have significantly detected (> 3σ), centrally-peaked, and compact (< 0.1 pc, 2" at our resolution) CH₃OH emission. To identify CH₃OH lines in the sources, we use astroquery to search the JPL Millimeter, Submillimeter, and Microwave Spectral Line Catalog (Pickett et al. 1998) for lines within the given spectral window using Splatalogue (astroquery, Ginsburg et al. (2016); Splatalogue, Markwick-Kemper et al. (2006)). Given its brightness, we examine the first spectral window for the 5_1-4_2 vt=0 transition of CH₃OH. Once identified, we use the doppler velocity of this line as a tentative velocity for the source. We then fit a single-component Gaussian to the line using the Levenberg-Marquardt least-squares fitter in astropy to obtain a precise doppler velocity for the $5_1 - 4_2$ line based on its primary velocity component.

Emission from low-J ($E_{upper} < 96 \text{ K}$) CH₃OH lines traces both compact sources and extended emission. As such, we choose the detection of the $10_{2-} - 9_{3-}$ line to mark hot core candidates $(E_{upper} = 165 \text{ K}, \text{ see Table 1}), \text{ as it}$ is the lowest-J transition that uniquely traces We additionally exclude compact sources. sources that are beyond the half-power beam width (HPBW) of our observations to minimize the effects of the primary-beam correction on our measurements. Temperature measurements performed on sources which are within and outside the HPBW in different fields show temperatures that are discrepant by factors of a few to several.

Once a candidate has been identified in the line data, we cross-correlate the position of the CH₃OH source to the 1 mm continuum data. We create square cutout images centered on the corresponding continuum peak that enclose the source and the surrounding 2–6.25" (0.08-0.25 pc). This prevents the inclusion of additional

Table 1. Detected CH₃OH Lines

Transition	Rest Frequency	E_U
	(GHz)	(K)
$5_1 - 4_2 \text{ E1}$	216.946	55
$6_{1-} - 7_{2-} v_t = 1$	217.299	373
$15_{6\pm} - 16_{5\pm} v_t = 1$	217.643	745
$20_1 - 20_0 \text{ E1}$	217.887	508
$4_2 - 3_1 E1$	218.440	45
$25_3 - 24_4 \text{ E1}$	219.984	802
$23_5 - 22_6 E1$	219.994	775
$8_0 - 7_1 \text{ E1}$	220.079	96
$10_{2-} - 9_{3-}$	231.281	165
$10_{2+} - 9_{3+}$	232.419	165
$8_6 - 8_7 \text{ E1 } v_t = 1$	232.645	675
$18_{3+} - 17_{4+}$	232.784	446
$14_6 - 14_7 \text{ E1 } v_t = 1$	232.925	835
$10_{-3} - 11_{-2} \text{ E}2$	232.946	190
$18_{3-} - 17_{4-}$	233.796	446
$13_{3-} - 14_{4-} v_t = 2$	233.917	868
$13_{3+} - 14_{4+} v_t = 2$	233.917	868

sources with different doppler velocity than the selected source, which would result in spurious temperature values after the following analysis steps are complete. For the source Sgr B2(S), which is comprised of multiple continuum sources sharing a molecular envelope, we center on the reference pixel from which we pulled spectra (see Table 2).

2.3. Measuring CH₃OH rotational temperature

As hot cores are chemically enriched and often show broad or complex velocity structure, there may be contamination by non-CH₃OH species that must be accounted for before beginning analysis. To mitigate the inclusion of contaminants, we examine the profiles of the CH₃OH lines in the source to identify a bright, isolated line from which to derive a representative velocity field for the gas. Lines that are

not fully blended (i.e., contaminants $\gtrsim 1\sigma$ line width separated from the chosen line) may also be used after limiting the range of included velocities to the primary emission component. We chose a different isolated reference line for each hot core. Frequently chosen transitions include $5_1 - 4_2$ vt=0, $8_0 - 7_1$ vt=0, and $20_1 - 20_0$ vt=0 (see Table 2). Once a reference line has been selected, we create spectral slabs centered on the measured velocity with widths equal to the FWHM of the representative line. We then apply a $3\sigma_{SC}$ signal mask to the slab, where σ_{SC} is the uncertainty on the continuum level derived from STATCONT. and compute the velocity field (moment-1) and FWHM (moment-2) maps of the core for use in forthcoming analysis steps.

We search for detections of methanol lines by creating LTE models at temperatures and column densities corresponding to our first rough estimates, i.e., T = 150 - 300 K and $N_{tot} = 0.1 1.0 \times 10^{17}$ cm⁻². We then compare the modeled intensity to the measured uncertainty at each frequency and select those transitions with predicted $> 3\sigma$ detections. We then ignore other lines of CH₃OH, such as those with high upperstate energy levels (several have $E_U \gtrsim 2000 \text{ K}$). Once a candidate line is identified, we check whether the data within the selected velocity range $(v_{center} \pm FWHM)$ have a peak intensity $T_{b,max} \geq 3\sigma_{SC}$. We calculate the integrated intensity of lines that meet this criterion and exclude others in the remainder of our modeling. The velocity ranges vary between sources, and we have indicated as such in the caption of each figure in the associated figure set (see Appendix A).

The spectra we analyze are continuumsubtracted. However, the continuum brightnesses in the hot cores can contribute between 20% to 40% of the line brightnesses, which dilutes the observed integrated intensity if not accounted for. We therefore apply a final correc-

tion for continuum dilution by adding the continuum brightness multiplied by the measured FWHM of each line to the integrated intensity. Using these corrected integrated intensity maps (see Appendix A), we calculate upper-state column densities of the lines using the following equation:

$$N_u = \frac{8\pi k_B \nu^2}{hc^3 A_{ij}} \int_{v_1}^{v_2} T_b dv$$
 (1)

where N_u is the upper-state column density, k_B is the Boltzmann constant, ν is the rest frequency of the transition, h is the Planck constant, c is the speed of light, A_{ij} is the Einstein A coefficient for the transition, and $\int_{v_1}^{v_2} T_b dv$ is the integrated intensity (Mangum & Shirley 2015). By dividing N_u by g_u , the degeneracy of the transition, and plotting with respect to the upper-state column density E_u , we construct per-pixel rotational diagrams for the detected CH₃OH transitions (Goldsmith & Langer 1999, see Figure 2).

To compute T_{rot} , we begin with the equation of N_u ,

$$N_u = \frac{N_{tot}g_u}{Q_{rot}} \left[\exp\left(\frac{E_u}{k_B T_{ex}}\right) \right]^{-1}$$
 (2)

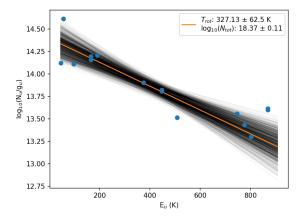
where Q_{rot} is the rotational partition function (Mangum & Shirley 2015).

Rearranging (2) and setting $T_{ex} = T_{rot}$, we use

$$\log_{10}\left(\frac{N_u}{g_u}\right) = \frac{-E_u}{k_B T_{rot}} \log_{10}(e) + \log_{10}\left(\frac{N_{tot}}{Q_{rot}}\right)$$
(3)

to calculate T_{rot} and construct maps of the gas temperature within a region of interest.

To compute the error on T_{rot} and N_{tot} , we initially compute the statistical error on the linear fit as derived by Hogg et al. (2010). However, this method produces T_{rot} error $(\sigma_{T_{rot}})$ values that do not appropriately capture the uncertainty implied by the observed scatter in the rotational diagrams (e.g., $\sigma_{T_{rot}} \lesssim 10$ K).



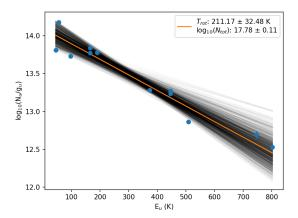


Figure 2. Rotational diagrams representative of the hot core envelope in Sgr B2(S) (upper) and over the hot core continuum peak from and DS2 (lower). The cores show N_u values (blue points) that are reasonably well fit by the LTE model (orange line), with some scatter. The black background lines show the LTE models derived from the bootstrapping method.

Some methanol transitions (e.g., the 5-4 line, see the second datapoint in Figure 2) show N_u/g values that consistently deviate from LTE predictions. We do not explore the apparent non-LTE excitation of these lines in this work. However, to account for the impact these deviations may have on our results, we employ a simple bootstrapping method using the astropy.stats.bootstrap package. In each pixel, we perform 1000 bootstrap resampling iterations. We refit the LTE model to each of these samples, and find that bootstrap samples

are reasonably approximated by a Gaussian distribution. We therefore take the standard deviation of the resulting N_{tot} and T_{rot} values to obtain the uncertainty estimate. We report these bootstrap errors in Table 3 and propagate them through all values derived from T_{rot} and N_{tot} .

2.3.1. The effects of CH_3OH opacity on T_{rot}

As the density of $\mathrm{CH_3OH}$ increases, the lower-J transitions will become optically thick and self-absorbed, causing the observed N_{tot} from the rotational diagrams to stop growing and the observed T_{rot} to increase. However, as $\mathrm{N(H_2)}$ may continue to independently increase, this can artificially decrease $\mathrm{X(CH_3OH)}$. We therefore set out to test the influence of line optical depth on our results.

Qualitatively examining the spectra from pixels showing this abundance decrease, we only find evidence of CH₃OH self-absorption in the 4-3 line in DS1, suggesting that τ_{CH_3OH} is not extremely high across the sample. To quantitatively characterize the influence of τ_{CH_3OH} on T_{rot} , we examine the line opacities over the pixel showing the highest T_b in the 4-3 line of each source. These regions are coincident with the continuum peaks for every source except Sgr B2(S), in which case we test the highest dust continuum peak and the T_{rot} peak. We use the measured N_{tot} value in the selected pixel and the lte_molecule module of pyspeckit to model the optical depth of each line over a range of fiducial hot core temperatures, as shown in Figure 3.

These models show a trend of increasing τ with N_u , with the highest values of τ reaching approximately 0.3 for the highest-opacity sources. To produce marginally optically thick lines consistent with our N_u measurements (i.e., $\tau \gtrsim 0.6$), the measured T_{rot} in the chosen pixel would need to be overestimated by a factor of 2 or more. Assuming we were underestimating the opacity in the lowest-J lines such that the true value of τ is of order 0.6, we apply the op-

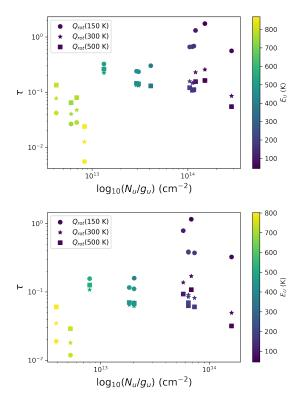


Figure 3. Line opacities for fiducial hot core temperatures of 150 K (circles), 300 K (stars), and 500 K (squares) for Sgr B2(S) (upper) and DS2 (lower). The color of the data points corresponds to the E_u value for each transition.

tical depth correction to our N_u measurements as given by Goldsmith & Langer (1999). We find that these modeled values of N_u differ from the values we measure with the optically thin approximation by 28.3%, equivalent to no more than a 10 K increase in the T_{rot} error we measure.

As an additional test, we are able to reasonably reproduce the spectra for the 23 identified species using our measured temperatures and estimates on their total column densities (see Section 3.1). Taken together, these results show that τ_{CH_3OH} does not significantly impact our measured temperatures and therefore is not a dominant factor in our analysis.

3. RESULTS

The general physical properties of each examined hot core are shown in Table 2. Source radii

were measured as the radius at which the azimuthally average temperature reached its minimum value or 150 K (R_{core}). We choose 150 K to be consistent with predictions for the sublimation temperatures of CH₃OH and frequently studied COMs with water ice ($\sim 120-160$ K, see Garrod et al. (2022)) and because we do not observe temperatures below 100 K in several cores, unlike what is found in canonical Galactic disk hot cores (e.g., Gieser et al. (2021)). Uncertainties on the radius were taken as the 1σ beam radius. Source masses were measured by computing the sum of the mass within each target's R_{core} .

Figure 4 shows the CH₃OH lines used to produce the temperature map for Sgr B2(S) and overplotted pyspeckit-modeled lines produced using the measured T_{rot} , N_{tot} , and line width in this pixel. The model reproduces the data well, with deviation from the model line brightnesses in some lines and slight velocity offsets in others. In some other sources, the models less convincingly reproduce the data, overpredicting the line brightnesses by factors of 2 to a few (e.g., Figure 17.3, see Appendix D). We attribute these deviations to limitations of our single-temperature, single-velocity assumption, as it is likely that the temperature and velocity structure of the cores changes on smaller scales.

In Figure 5, we show maps of the number of detected CH_3OH transitions $(n_{transition})$ per pixel for Sgr B2(S) and DS1. These maps are characteristic of the DS hot core population, showing excited CH_3OH that is both cospatial with regions of 1 mm dust continuum and spans several thousand AU away from the primary continuum features. Peak $n_{transition}$ values overlap with regions of highest continuum emission and are roughly constant across these same regions. $n_{transition}$ maps for the remaining hot cores are shown in Appendix B.

$3.1. \ Temperatures$

Examples of rotational diagrams from Sgr B2(S) and DS1 are shown in Figure 2. Peak temperatures for the full sample are shown in Table 3. Sample temperature maps from Sgr B2(S) and DS2 are shown in Figure 6, with those of the remaining sources shown in Appendix C. All temperature maps only include temperatures $T_{rot} \geq 3\sigma_{T_{rot}}$. A majority of the cores (seven of 10) show temperature peaks within one beam width of the core's continuum peak. In Sgr B2(S), local temperature peaks are similarly present over its constituent continuum peaks. In DS7 and DS9, hot ring features surround the continuum peaks.

We note that the 5-4 transition is higher than our LTE model predicts (see e.g., the second data point in both panels of Figure 2). The effects of this line are accounted for in the bootstrapping uncertainty estimation we employ (see Section 2.3), as removing it produces less than a 1σ difference in our temperatures. Similar plots for the remaining hot cores are shown in Appendix D.

Appendix E shows continuum-subtracted ALMA spectra of all four spectral windows from the representative pixel of the observed hot cores. Overplotted are pyspeckit-modeled lines produced by CH₃OH and a sample of identified species at the measured $T_{rot}(CH_3OH)$ in the chosen pixels. We select these sources to illustrate the range of line densities and brightnesses present within the sample. We assume all molecules have a common T_{rot} based on the qualitatively similar line widths in various species, which we interpret to mean they are coming from similar parcels of gas in the envelope. At the same time, we note that this is meant as an initial estimate. Based on these assumptions, we identify 25 unique molecular species (including isotopologues), and one vibrationally excited species ($HC_3N \ v7 = 1$). Among the identified species, 11 are COMs: CH₃OH, ¹³CH₃OH,

Table 2. Observational properties of the Sgr B2(DS) hot cores. Uncertainties on each core's RA and DEC are given in parentheses and equivalent to one beam width. Velocities are the line of sight velocity measured from each source's representative line.

Source Name	RA (ICRS (J2000))	DEC (ICRS (J2000))	Systemic Velocity	Representative Line
	(hh:mm:ss.ss)	(dd:mm:ss.ss)	$({\rm km~s^{-1}})$	
Sgr B2(S)	17:47:20.48(0.02)	-28:23:46.3(0.3)	69.3	$20_1 - 20_0 \text{ E1}$
DS1	17:47:19.58(0.02)	-28:23:49.9(0.3)	56.2	$8_0 - 7_1 \text{ E1}$
DS2	17:47:20.05(0.02)	-28:23:46.7(0.3)	48.7	$8_0 - 7_1 \text{ E1}$
DS3	17:47:19.99(0.02)	-28:23:48.9(0.3)	52.8	$10_{2-} - 9_{3-}$
DS4	17:47:19.77(0.02)	-28:23:43.5(0.3)	54.6	$20_1 - 20_0 \text{ E1}$
DS5	17:47:19.71(0.02)	-28:23:51.6(0.3)	55.1	$8_0 - 7_1 \text{ E1}$
DS6	17:47:21.12(0.02)	-28:24:18.3(0.3)	49.8	$8_0 - 7_1 \text{ E1}$
DS7	17:47:22.23(0.02)	-28:24:34.0(0.3)	48.7	$8_0 - 7_1 \text{ E1}$
DS8	17:47:22.04(0.02)	-28:24:42.6(0.3)	49.8	$8_0 - 7_1 \text{ E1}$
DS9	17:47:23.46(0.02)	-28:25:52.1(0.3)	47.3	$8_0 - 7_1 \text{ E1}$

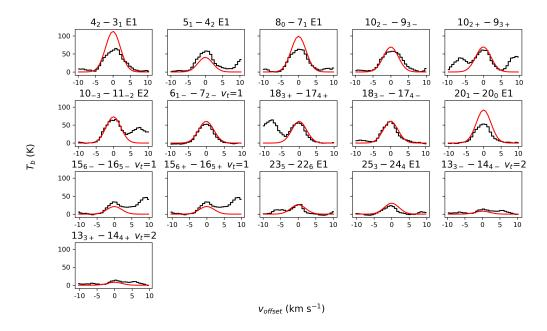


Figure 4. Spectra of the CH₃OH lines used to produce the temperature maps for Sgr B2(S) from its representative pixel. Black lines are the ALMA 1 mm measurements, and red lines are LTE model lines computed using our measured T_{rot} , N_{tot} , and line widths. The model reproduces the data well, with some deviation from predicted brightnesses and slight offsets from the systemic velocity of the source. These variations are present with different lines across the data set, which we attribute to limitations of our single-temperature, single-velocity assumption.

JEFF ET AL.

Table 3. Measured properties for the Sgr B2(DS) hot cores.

Core	T_{peak}	$N^a_{tot,max}$	R_{core}	$N_{H_2,max}^a$	M_{core}	$X(CH_3OH)_{peak}$
	(K)	$(\times 10^{17} \text{ cm}^{-2})$	(AU)	$(\times 10^{24} \text{ cm}^{-2})$	$({ m M}_{\odot})$	$(\times 10^{-7})$
DS1	306 ± 75	14.22 ± 0.45	5004 ± 1489	1.70 ± 0.03	874 ± 67	8.44 ± 1.61
DS2	239 ± 41	5.81 ± 0.18	3753 ± 1489	0.69 ± 0.11	423 ± 31	8.54 ± 1.48
DS3	351 ± 47	6.49 ± 0.62	5838 ± 1489	1.83 ± 0.32	1568 ± 104	3.8 ± 0.7
DS4	398 ± 57	10.68 ± 1.06	4881 ± 1489	1.35 ± 0.21	843 ± 65	7.74 ± 1.42
DS5	357 ± 90	1.75 ± 0.16	3934 ± 1489	0.62 ± 0.10	420 ± 36	3.5 ± 0.8
DS6	427 ± 69	12.33 ± 0.21	6672 ± 1489	2.22 ± 0.47	2192 ± 125	6.11 ± 1.18
DS7	282 ± 51	4.7 ± 0.18	4107 ± 1489	1.37 ± 0.30	612 ± 51	3.4 ± 0.8
DS8	300 ± 42	3.59 ± 0.41	3587 ± 1489	0.69 ± 0.10	287 ± 25	5.31 ± 1.0
DS9	252 ± 39	2.42 ± 0.14	3956 ± 1489	0.38 ± 0.06	203 ± 16	6.49 ± 1.12
SgrB2S	662 ± 191	23.56 ± 0.62	9436 ± 1489	3.01 ± 0.60	4842 ± 787	11.31 ± 1.76

^aPeak N_{tot} values and peak N_{H_2} are pulled from different pixels.

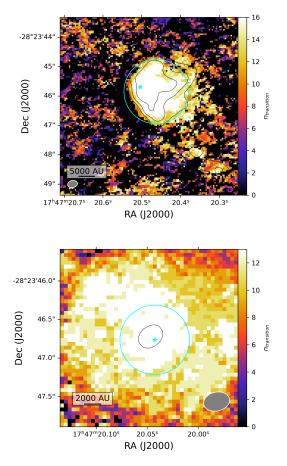
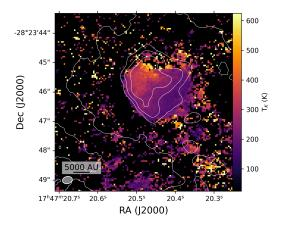


Figure 5. CH₃OH $n_{transition}$ maps for Sgr B2(S) (upper) and DS2 (lower). Black contours show the 1mm dust continuum emission at 3, 6, 8, 12, and 32σ . Cyan stars mark the position of the represenative pixel for each source, and the cyan circles mark R_{core} . Both cores show CH₃OH emission spanning several thousands AU away from the continuum, with peak $n_{transition}$ values overlapping with the continuum. Peak $n_{transition}$ values are broadly constant across the continuum overlap regions. Sgr B2(S) has a higher excitation state than DS2, based on $n_{transition}$, and this excitation extends almost uniformly throughout the main body of the core. In addition, there are regions to the south which are also highly excited. DS2 shows a similar uniform excitation throughout its extent.

¹³CH₃CN, CH₃CHO, CH₃NCO, CH₃OCHO, CH₃OCH₃, C₂H₅OH, NH₂CHO, CH₂CHCN, and CH₃CH₂CN. While many lines remain unidentified, the hot cores show a similar dis-



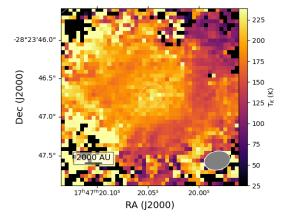


Figure 6. CH₃OH rotational temperature maps for Sgr B2(S) (upper) and DS2 (lower). White contours show the 1 mm dust continuum and the contour levels are 3σ , 6σ , 8σ , 16σ , and 32σ ($\sigma=0.2$ mJy beam⁻¹). The hot gas within Sgr B2(S) spans a large area (~ 0.5 pc across its horizontal) and is dominated by the distinct hotspot in its northeast. DS2 shows a more uniform morphology, with an extended envelope of warm (~ 200 K) gas surrounding its continuum. Temperature maps for the remaining cores can be found in Appendix C.

tribution of species across the identified COMs, as eight of these 10 species are detected in each core. Assumed total column densities for each species are manually tuned to match the data, and there is good agreement (T_b within factors of a few) between the models and the dataset.

With these detections, we now have reasonable templates for hot cores that we can use for further, deeper searches in the data.

3.2. Core physical structure

As noted in Section 1, Sgr B2 provides a valuable laboratory within which to explore the resolved properties of stars forming in conditions resembling those found near the peak of cosmic star formation. In detail, the structural properties (i.e., the thermal and density gradients) of CMZ's massive protostars are relatively unexplored. These properties are of particular importance, as they inform modeling of the physical and chemical evolution of massive protostars (see e.g., (van der Tak et al. 2000)). To begin investigating these quantities in our sample, we follow Gieser et al. (2021), who created radial power-law indices to model the physical characteristics of a catalogue of hot cores in the Galactic Disk. In the following subsection, we briefly discuss radial temperature and density profiles and power-law fits we created to facilitate comparison between Deep South and this catalogue (see Section 4.2).

3.2.1. Radial temperature profiles

We constructed radial temperature distributions for each core, with those of Sgr B2(S) and DS1 shown in Figure 7. We initially fit single power-law profiles to these distributions, as described by the following equation:

$$T_{rot}(r) = A \left(\frac{r}{r_{break}}\right)^{-\alpha}$$
 (4)

where A is the normalization constant, r is the radial distance from the hot core continuum peak, r_{break} is the break point of the power law, and α is the single power-law index. However, these profiles are a poor fit to the data for $r \lesssim 4000$ AU. To better parameterize the data, we fit broken power-law profiles to the data using the following equation:

$$T_{rot}(r) = A \left(\frac{r}{r_{break}}\right)^{-\alpha_1} : r < r_{break}$$

$$A \left(\frac{r}{r_{break}}\right)^{-\alpha_2} : r > r_{break}$$
(5)

where α_1 and α_2 are the interior and exterior power-law indices, respectively. We find that broken power laws better describe the behavior towards the interiors of the hot cores, where the temperatures initially fall slower than single power laws predict.

Table 4 reports the parameters of the broken power-law fits for each hot core in the sample. The temperature distributions for hot cores DS2 through DS9 are shown in Appendix F. We compare α_2 to similar measurements performed on in the Galactic Disk CORE survey in Section 4.2.

3.2.2. Radial density profiles

To compute densities for our sample, we first set the dust temperature $T_{dust} = T_{rot}$. While the dust temperatures are not well known at these scales, they should be thermally coupled to the gas (Clark et al. (2013)) in the expected density regime of the hot cores ($n \gtrsim 10^7$ cm⁻³; e.g., Motte et al. (2018)). We then compute the peak dust optical depth for each source using the following equation:

$$\tau = \frac{S_{\nu}c^2}{2k_B T_{rot}\nu^2} \tag{6}$$

where S_{ν} is the dust surface brightness in Kelvin, c is the speed of light, and ν is the representative frequency of the continuum. The highest value of τ among the hot cores is 0.07, meaning optically thin dust. We then derive H_2 column densities $N(H_2)$. Using the continuum brightness temperatures T_B and again setting $T_{dust} = T_{rot}$, we arrive at the following equation:

$$N(H_2) = \frac{T_b \Omega D^2 c^2}{2k_B \nu^2 \kappa_\nu \mu A_{beam} T_{rot}}$$
 (7)

where $\Omega=2.79\times 10^{-12}$ sr is the beam solid angle, D=8.34 kpc is the distance to Sgr B2 , c is the speed of light, $\nu=217.35$ GHz is the representative frequency of the continuum, mean

Core	α_1	$lpha_2^\dagger$	r_{break}	p
DS1	0.15 ± 0.03	0.36 ± 0.01	1931 ± 224	1.9 ± 0.008
DS2	0.07 ± 0.04	0.15 ± 0.01	1719 ± 547	1.06 ± 0.01
DS3	0.04 ± 0.08	0.31 ± 0.03	1533 ± 362	1.64 ± 0.01
DS4	0.11 ± 0.06	-	-	1.886 ± 0.008
DS5	0.18 ± 0.17	1.17 ± 0.11	2637 ± 331	1.26 ± 0.02
DS6	0.1 ± 0.2	0.36 ± 0.02	1029 ± 439	1.689 ± 0.003
DS7	-0.05 ± 0.07	0.65 ± 0.03	1844 ± 113	1.714 ± 0.008
DS8	0.1 ± 0.09	0.55 ± 0.08	1943 ± 323	1.72 ± 0.01
DS9	0.55 ± 0.08	0.31 ± 0.08	4293 ± 895	1.65 ± 0.01
Sgr B2(S)	0.17 ± 0.04	0.58 ± 0.08	5444 ± 561	2.05 ± 0.01

Table 4. Fitted parameters of the radial temperature profiles for each hot core.

molecular weight $\mu=2.8$ (Kauffmann et al. 2008), and A_{beam} is the beam area in AU at the distance of Sgr B2. We choose a distance of 8.34 kpc to Sgr B2 to maintain consistency with Schmiedeke et al. (2016) (see Section 4.1). The opacity constant $\kappa_{\nu}=0.008~{\rm cm^2~g^{-1}}$ (Ossenkopf & Henning 1994) implicitly assumes a gas-to-dust ratio of 100. We include N(H_2) maps for each source in Appendix G.

Using our $N(H_2)$ measurements, we create radial density profiles assuming spherical symmetry for each hot core (e.g., Figure 8). We fit single power law profiles to each distribution following Equation 4 and report the fitted power law index p in Table 4. Peak densities in all cores are approximately 10^{10} cm³. We note here that lower dust temperatures would imply a higher optical depth. However, this would act to increase the densities we measure or make them lower limits, if the cores were optically thick. This implies that T_{dust} is strongly coupled to the gas temperatures in our sources (e.g.,

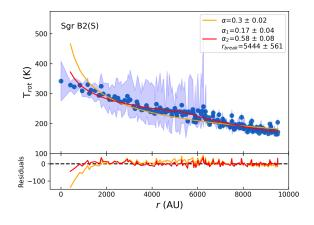
Clark et al. (2013)). In these conditions and at our resolution, the dust within the hot cores is optically thin with values $\tau < 0.07$. We discuss p and how it compares between DS and a selection of Galactic Disk hot cores in Section 4.2.

3.3. Abundances

Using the $N(H_2)$ measurements described in Section 3.2.2, we create methanol abundance (X(CH₃OH)) maps by taking the ratio $N_{tot}/N(H_2)$ (see Table 2 for peak N_{tot} and $N(H_2)$ values). Abundance maps for Sgr B2(S) and DS2 are shown in Figure 9, and those of the other sources are shown in Appendix H.

The hot core Sgr B2(S) contains an HII region in its northern regions (e.g., Lu et al. (2019); Meng et al. (2022)). As free-free contamination of the continuum is a concern in this region, we omit the HII region when measuring the abundances in this source. There are no free-free detections in the remaining hot cores.

[†]We set $\alpha_2 = q$ in the lower panel of Figure 14, except in DS4, DS9, and Sgr B2(S). We use α_1 for these sources as the temperature profile is well described by this value until relatively large radii (i.e. r_{break} for this source). In DS4, its measurements of α_2 and r_{break} are not statistically significant, so we omit them with dashes.



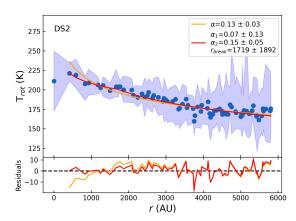
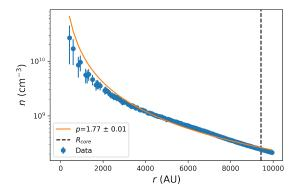


Figure 7. Radial temperature profiles for Sgr B2(S) (upper) and DS2 (lower). As Sgr B2(S) contains multiple continuum sources, its profile is centered on its temperature peak. DS2 is centered on the peak of its continuum. Both cores show clear peaks indicative of central heating, however Sgr B2(S) has a significantly warmer temperature peak. Overplotted are single (orange) and two-component broken (red) power law fits as described in Section 3.1. The residuals to the power law fits are shown in the lower panels in each plot.

We qualitatively identify a trend of increasing abundance with T_{rot} across the sample. However, there is variation on a source-by-source basis: we do not observe a common peak abundance value, or a common temperature at the abundance peak in any hot core. Temperatures at the abundance peaks range from ~ 200 to 400 K. A majority (DS1-DS9) of the sources show monotonic increases in abundance until



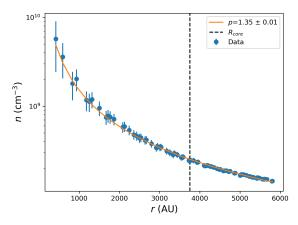
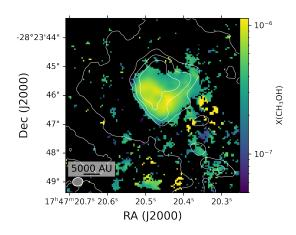


Figure 8. Radial density profiles for Sgr B2(S) and DS2. The orange line is our single power law fit for each source, and we report the associated power law index p using the same nomenclature as Gieser et al. (2021). The vertical black line shows R_{core} for each source.

the highest measured temperatures. However Sgr B2(S) (upper panel in Figure 10) is unique in the sample, as its abundance rises to a peak at 210 K, and then flattens to a roughly constant value out to the highest temperatures for which we have abundance measurements. The individual $X(CH_3OH)$ vs T_{rot} distributions of the remaining hot cores are shown in Appendix I.

To compare the abundance behavior of each DS hot core in the sample, we plot a kernel density estimate of the abundances and temperatures for each source in Figure 11. The increasing abundance trend is visible here, with scatter in the distribution arising from the unique abundance behavior in each hot core. We briefly



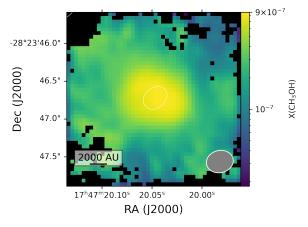


Figure 9. CH₃OH abundance maps for Sgr B2(S) (upper) and DS2 (lower). Regions in which the 1 mm continuum (white contours) is detected at less than 3σ have been masked out.

discuss potential physical drivers for these results and compare the peak abundances in Deep South to those of hot cores in other regions of Sgr B2 and the Galaxy in Section 4.3.

In Figure 12, we show radial abundance profiles for the full hot core dataset. In all of our sources, we identify a trend of decreasing CH₃OH abundance with separation from the dust continuum cores, with some scatter depending on the abundance morphology of individual sources. This is broadly consistent with the canonical image of hot cores, where thermal feedback from embedded protostars sublimates the grain mantles in the protostellar envelope.

4. DISCUSSION

The hot cores of Sgr B2(DS) are a heterogeneous population with a range of temperatures, masses, abundances, and structural properties. In the following sections, we discuss these sources in the context of other hot core populations in the Galaxy, including those within Sgr B2, and what our results suggest about the recent epoch of star formation in Sgr B2.

4.1. Sgr B2(S): a younger Sgr B2(N) and (M)?

Schmiedeke et al. (2016)use threedimensional modeling of archival millimeter and FIR datasets from the Very Large Aarray, APEX, Submillimeter Array, and Herschel to derive a stellar cluster radius of 0.35 pc for Sgr B2(S). Within this radius, we quote their measured H_2 mass of 4472 M_{\odot} . Our higherresolution observations in the millimeter regime reveal a cluster of hot cores neighboring Sgr B2(S) within this same radius (sources DS1 through DS5), which we have named the Deep South Hot Core Complex. The newly discovered hot cores contain a total molecular gas mass of 4128 M_{\odot} , yielding combined molecular gas mass with Sgr B2(S) $(M_{core} = 4842 \text{ M}_{\odot})$ of 8970 M_{\odot} . These measurements show that Sgr B2(S) dominates the flux at 3 mm and 1 mm flux in this region. However, it only contains just over half (54%) of the total high-mass starforming mass. The remaining 46% is located in the cooler, less luminous complex members (DS1-DS5).

These results nearly double the mass in highmass stars in the vicinity of Sgr B2(S), and there are numerous currently uncatalogued lowermass or less evolved cores distributed in the same region. We therefore suggest that, instead of Sgr B2(S) being a less massive sibling to Sgr B2(N) and (M), it and the neighboring hot cores throughout the complex may instead comprise a younger, comparably massive sibling.

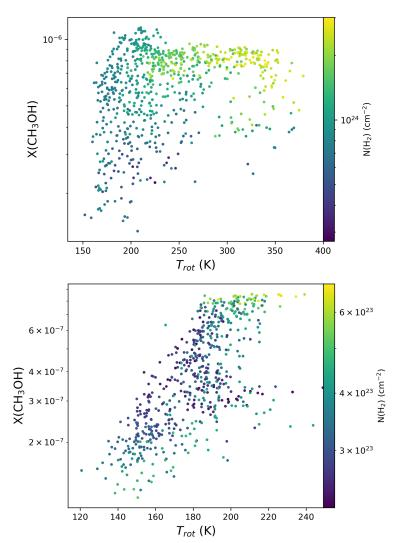


Figure 10. Abundance vs. temperature plots for DS2 (left) and Sgr B2(S) (lower) showing the variation in abundance behavior across sources. Each point represents a single pixel. In DS1, the abundance increases monotonically with temperature until the temperature peak is reached. In Sgr B2(S), X(CH₃OH) peaks near 210 K before descending to a constant value at higher temperature. The abundance vs temperature plots for the remaining hot cores can be found in Appendix I.

4.2. Comparison to Galactic disk hot cores

We compare the properties of the DS hot core population to a selection of Galactic disk hot cores studied at comparable (~ 3000 AU) resolution in WB 89789, (Shimonishi et al. 2021) and in the CORE survey (Gieser et al. 2021), and at comparable temperatures in W51 (Goddi et al. 2020). The masses reported in Table 3 of Gieser et al. (2021) were derived using a gas to dust ratio $\frac{M_{gas}}{M_{dust}}=150$ and an opacity constant $\kappa=0.009~{\rm cm^2~g^{-1}}$ at 1.3 mm. These differ from

the values we assume in this work ($\frac{M_{gas}}{M_{dust}} = 100$, $\kappa = 0.00858941$ cm² g⁻¹ at 1.3 mm; Ossenkopf & Henning (1994)), thus we scale their masses to allow for direct comparison to those of Deep South. The scaled masses differ from the values reported in Gieser et al. (2021) by 8.9%.

In the upper panel of Figure 13, we plot the distribution of peak temperatures as a function of core mass. The DS hot cores have masses and temperatures that are similar to the W51 cores, however they are more massive and generally

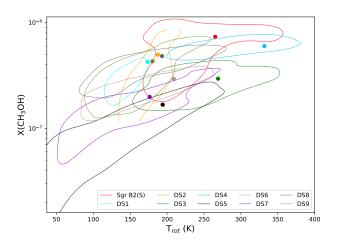


Figure 11. Diagnostic plot showing the distribution of $X(CH_3OH)$ as a function of T_{rot} for the DS hot cores. Contours show the distribution of abundances in each hot core as a function of temperature. They show a positive correlation with temperature, with scatter attributed to core-specific chemical evolution. Colored points correspond to the signal-to-noise-weighted averages, where the weights are the signal-to-noise of the abundance for each hot core.

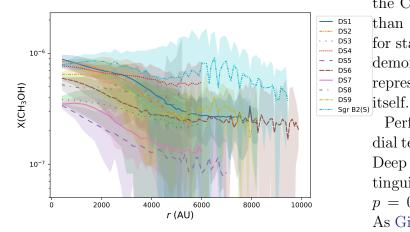
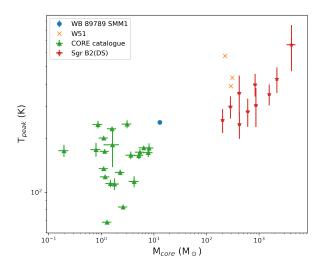


Figure 12. Radial abundance profiles for the full sample of hot cores in this work. The profiles were smoothed with a median kernel of 3. Shaded regions show the 1σ distribution of abundances for each radial bin. All sources have a decreasing abundance distribution out to large radii, consistent with typical models of hot cores.

warmer than the rest of the comparison set. In the lower panel of Figure 13, we also find that the DS cores have radii that are broadly consistent with those of the Galactic disk.

We compare the measured radial density profiles p (Section 3.2.2) to similar measurements done on the CORE catalogue. We find that the DS hot cores have, on average, shallower $(p = 1.66 \pm 0.01)$ density profiles than the CORE catalogue ($p = 1.85 \pm 0.09$, Gieser et al. (2021); see Figure 14, upper panel). This means that, at a given radius, the DS hot cores are typically denser than the CORE hot cores, which aligns with the work of other authors concerning the threshold of star formation in the CMZ (see Henshaw et al. (2023) for recent review). The CMZ shows evidence of a higher surface density threshold for star formation than canonical dense-gas relations predict (e.g., Gao & Solomon (2004); Lada et al. (2012)). The origins of this result are heavily debated due to its impact on the stellar initial mass function, but a clear answer has yet to be revealed. Qualitatively, however, it follows that protostars in the CMZ would show evidence of being denser than the disk if the surface density threshold for star formation is higher, as our observations demonstrate. For now, it is not clear if DS is representative of Sgr B2, the CMZ, or an outlier

Performing the same comparison on the radial temperature power-law indices, we find that Deep South's hot cores are statistically indistinguishable from the CORE catalogue, with $p = 0.44 \pm 0.04$ and 0.51 ± 0.08 , respectively. As Gieser et al. (2021) did not observe a broken power-law behavior and our measured α_1 only applies to the inner $\lesssim 3000$ AU of our cores, we compare q to our α_2 in the lower panel of Figure 14. We use α_1 in DS4, DS9, and Sgr B2(S) since their radial temperature profiles are well fit by this index out to large radii. We can use this result to make inferences about the structure



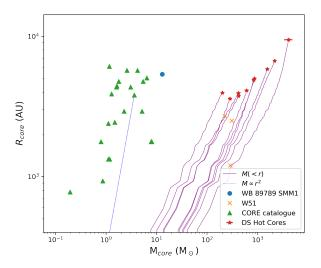


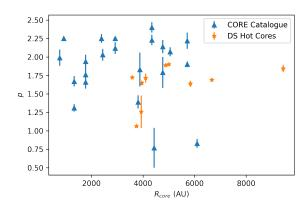
Figure 13. Comparison plots showing the distribution of peak temperatures (upper) and radii (lower) as a function of mass for the source studied in this work and a selection of Galactic disk hot cores which were studied at comparable resolution. The blue circle represents hot core WB 89789 SMM1 (Shimonishi et al. 2021), green triangles are hot cores in the CORE catalogue (Gieser et al. 2021), yellow crosses are from the W51 region (Goddi et al. 2020), and red stars are the DS hot cores. Purple lines show the mass interior to each radial bin for each DS hot core. The blue dotted line is an $M \propto r^2$ profile as a reference.

of the cores on scales smaller than our resolution. van der Tak et al. (2000) use submillimeter continuum and molecular line observations and modeling to study the structural properties of a collection of massive YSOs in the Disk. Among the results in their work, they find radial temperature power-law indices which apply on comparable size scales to our work ($\gtrsim 2000 - 3000$ AU) and with which our observations also agree. The overlap in these results lets us infer that the DS hot cores have increasingly optically thick interiors starting on the scale of $\sim 1000 \text{ AU}$ and the thermal profile likely rises steeply on these size scales. Studying the temperatures on these size scales would require additional observations in Deep South, but the suggestion that the cores begin becoming optically thick on 1000 AU scales aligns with work published by Budaiev et al. (2024) in Sgr B2(N). Higherresolution, lower-frequency observations would likely allow us to begin probing this regime directly and elucidating the structure of these objects on the scales of their protostellar disks (e.g., Beltrán & de Wit (2016)).

Taken together, in spite of the extreme environment of Sgr B2, we find that the hot cores of Deep South overall share structural properties with our chosen hot core comparison set. The sources are have similar radii and show evidence of having similar interior structures on the scales of their protostellar disks. However, they are also typically warmer than the comparison set, and their radial density power-law indices hint at the influence of the higher star formation threshold present in the CMZ. Future studies on YSOs in Deep South, Sgr B2(N), and elsewhere in the CMZ will help clarify if these results are representative of CMZ star formation or if Deep South is unique.

4.3. The relative age of Sgr B2(DS)

The onset of star formation in Sgr B2 has been a point of interest in characterizing the star formation history of the CMZ and its broader ge-



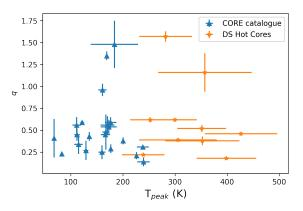


Figure 14. Plots comparing the fitted physical parameters of the CORE catalogue (Gieser et al. 2021) and the DS hot cores. Upper panel: distribution of density power law indices (p) as a function of R_{core} . Our sample shows an average shallower distribution of p than their CORE counterparts. Lower panel: distribution of radial temperature indices (q) as a function of peak temperature. We compare q to α_2 in this work due to the resolution limits of the CORE survey. The DS hot cores have radial temperature index distribution that is statistically indistinguishable from the CORE catalogue.

ometry (e.g., Kruijssen et al. 2015; Henshaw et al. 2016), in addition to the physical and chemical history of Sgr B2 itself (e.g. Ginsburg et al. 2018; Bonfand et al. 2019; Meng et al. 2022). Meng et al. (2022) place constraints on the relative timescale for star formation in Sgr B2 by observing the distribution of UCHII regions relative to dust sources throughout the cloud. They report that S and DS are likely the youngest regions in the cloud, as they contain

the lowest number of UCHII regions (three) relative to N (eight) and M (40). By examining the characteristics of hot cores across the cloud, we explore an additional lens for determining relative age across Sgr B2, since hot cores represent a younger phase in massive protostellar evolution. We find that Sgr B2(DS) is not at an obviously different evolutionary stage than N, with several cores sharing features with those of N.

Sánchez-Monge et al. (2017) identify 14 and 12 hot core candidates between Sgr B2(N) and (M), respectively (chemically "rich" and "rich?" sources in their Table 4). In N, three of their sources had been previously identified as hot cores: N1 (AN01) and N2 (AN02 and AN03, Belloche et al. (2008, 2016)). Two more were confirmed and a new hot core was detected in observations by Bonfand et al. (2017): N3 (AN08), N4 (AN14), and N5. The candidates in Sgr B2(M) have not yet been examined to the level of detail as the cores in N and in this work.

Bonfand et al. (2017) proposed a tentative evolutionary sequence in which the presence of Class II CH₃OH masers (see Sobolev et al. (1997)) and absence of outflows and UCHII regions may indicate less evolved sources. Investigating the outflows in DS is beyond the scope of this current work, but we are able to examine the presence of UCHII regions and masers. Sgr B2(S) and N1 are likely the most evolved sources between these two regions, as they contain UCHII regions with no CH₃OH masers. Three DS hot cores contain masers and no UCHII region, as in N3 and N5, suggesting they may be at intermediate evolutionary stage: DS2, DS6, and DS8 (e.g., Houghton & Whiteoak 1995; Caswell 1996; Lu et al. 2019). The remaining sources have neither UCHII regions nor CH₃OH masers, making their relative ages unclear using this sequence.

However, in addition to studying the outflows, we may learn more about their relative evolutionary state by examining masers in other species. DS1 and DS2 are associated with rare 4.83 GHz H₂CO masers (sources D and G in Mehringer et al. (1994), reidentified as sources F4 and F5 in Lu et al. (2019)). The pumping mechanism of this maser is still poorly understood, however recent results suggest it may be associated with high-mass star formation (van der Walt & Mfulwane 2022). As DS2 is a source that contains both a Class II CH₃OH maser and H₂CO maser, it presents a unique opportunity to study maser mechanisms, their relationship to outflows, and to use them to infer the evolutionary state of high-mass protostars.

4.4. Deep South's methanol abundances in the Galactic context

As discussed in Section 3.3, while we observe abundance increasing with temperature in every source, there are source-specific differences in peak abundance and peak temperature. To examine how these differences compare in the broader picture of Milky Way hot cores, we compare peak abundance values as a function of coincident temperature to a selection of hot cores in Sgr B2 (Sgr B2(N1), Busch et al. (2022); Sgr B2(N2-N5), Bonfand et al. (2017)), the Disk (W51, Ginsburg et al. (2017); Orion KL, Crockett et al. (2014)), and the outer Galaxy (WB 89789 SMM1, Shimonishi et al. (2021)) in Figure 15. These cores were selected on the basis of having methanol abundance measurements at comparable spatial resolution ($\sim 5000 \text{ AU}$), which probes similar physical and chemical conditions to our work. We note that the two points from Sgr B2(N1) are taken from regions ~ 1 " offset from the continuum peak in that source, as the peak of the continuum is optically thick at the measured frequencies ($\sim 99 \text{ GHz}$). Busch et al. (2022) also employ two tracers to measure H_2 column density used in their abundances: dust continuum and $C^{18}O$. For consistency with

our work, we use the abundances they measure using the dust-derived H_2 column density (see Table 3 in their work).

The resultant distribution shows hints of a negative correlation between peak CH₃OH abundance and coincident T_{rot} , qualitatively consistent with predictions made in the codesorption with water-ice model discussed in Bonfand et al. (2019) Garrod et al. (2022). model the time-dependent chemical evolution of the hot cores Sgr B2(N2-N5) in order to constrain the physical conditions that led to the chemical abundances observed in those cores. They found that relatively high dust temperatures (> 25 K) and a slightly lower cosmic-ray ionization rate than predicted for the CMZ is needed to reproduce the observed abundances of CH₃OH and other COMs in their work. Given the similar peak abundance and coincident temperature in several DS hot cores, this may suggest similar physical conditions were present during their formation. The conditions responsible for the abundances we observe at higher temperatures ($\gtrsim 250$ K), conversely, are less clear. Per Garrod et al. (2022), reactions with H₃O⁺ and other species are predicted to decrease CH₃OH abundance at temperatures beyond the desorption of water ice ($\gtrsim 200 \text{ K}$). Instead, we observe a roughly constant distribution of abundances (to within factors of a few) across DS and a peak abundance that is nearly an order of magnitude higher than DS in W51 e2. This suggests that there are hightemperature formation pathways for CH₃OH, or that its destruction mechanisms are inhibited at these temperatures. Time-dependent modeling of the full chemical composition of the DS hot cores and the other cores in this comparison set would likely shed light on these questions, as would a larger sample of hot cores with which to compare.

5. CONCLUSIONS

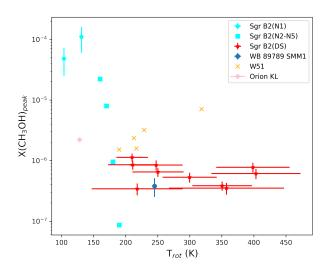


Figure 15. Peak CH_3OH abundance $(X(CH_3OH)_{peak})$ versus conincident rotational temperature for the hot cores studied in this work and a selection of hot core populations in the CMZ and Galactic Disk. $X(CH_3OH)_{peak}$ occurs at a wide range of T_{rot} , with further variation within individual populations. There may be hints that peak abundance decreases with temperature.

In this work, we report the discovery and resolved physical properties of nine new hot molecular cores throughout Sgr B2(DS) and the hot core Sgr B2(S). We summarize our main results here:

• These measurements reveal sources that have structural properties that are consistent with hot cores in the Galactic disk, with comparable radii and indications of similar interior structure below our resolution limit. However, our sample is also more massive and somewhat warmer than hot cores with similar measurements in the Galactic Disk, and has an average shallower distribution of radial density power-law result may be evidence of the effects of the higher surface density threshold for star formation in the CMZ.

- CH₃OH abundances generally decrease with distance from the hot cores and show a positive correlation with temperature across the full sample, consistent with the canonical picture of protostellar thermal feedback sublimating COMs in their envelopes. Comparing peak abundance in DS to those other other regions in Sgr B2 and the Galaxy, we find a relationship that qualitatively agrees with recent chemical modeling of massive protostars. However, we observe a high-temperature level-off in peak abundance, which suggests there are additional mechanisms of producing or preserving methanol which have yet to be explored.
- We find that a subset of Deep South hot cores shares physical characteristics (e.g. Class II CH₃OH masers, UCHII regions) with hot cores found in Sgr B2(N), suggesting these cores may be at similar evolutionary stages. Three of the discovered hot cores are associated with Class II CH₃OH masers, and two are associated with 4.83 GHz H₂CO masers.
- Five of our newly discovered hot cores and Sgr B2(S) exist in a radius of 1 pc and include a total H₂ mass of at least 8.9 × 10³ M_☉. Taken with the many lower-mass YSOs in this radius, our results suggest that Sgr B2(S) and nearby hot cores may be a less evolved but comparably massive cluster to Sgr B2(N) and (M). This makes (DS) a region of interest for studying the early phases of massive cluster formation.

6. ACKNOWLEDGEMENTS

We thank the anonymous referee for their constructive comments and suggestions which greatly improved the quality of this work. This paper makes use of the following ALMA data: ADS/JAO.ALMA#2017.1.00114.S. ALMA is a partnership of ESO (representing its member

states), NSF (USA) and NINS (Japan), together with NRC (Canada), MOST and ASIAA (Taiwan), and KASI (Republic of Korea), in cooperation with the Republic of Chile. The Joint ALMA Observatory is operated by ESO, AUI/NRAO and NAOJ. The National Radio Astronomy Observatory is a facility of the National Science Foundation operated under cooperative agreement by Associated Universities, Inc. Support for this work was provided by the NSF through the Grote Reber Fellowship Program administered by Associated Universities, Inc./National Radio Astronomy Observatory. A.G. and D.J. gratefully acknowledge support from NSF grant 2008101 and from the NRAO under the SOS program. A.G. acknowledges support from the NSF under grants 2142300 and 2206511. M.B. is a postdoctoral fellow in the University of Virginia's VICO collaboration and is funded by grants from the NASA Astrophysics Theory Program (grant number 80NSSC18K0558) and the NSF Astronomy & Astrophysics program (grant number 2206516). C.B. gratefully acknowledges funding from National Science Foundation under Award Nos. 1816715, 2108938, 2206510, and CAREER 2145689, as well as from the National Aeronautics and Space Administration through the Astrophysics Data Analysis Program under Award No. 21-ADAP21-0179 and through the SOFIA archival research program under Award No. 09_0540. A.S.-M. acknowledges support from the RyC2021-032892-I grant funded by MCIN/AEI/10.13039/501100011033 and by the European Union 'Next GenerationEU'/PRTR, as well as the program Unidad de Excelencia María de Maeztu CEX2020-001058-M, and support from the PID2020-117710GB-I00 (MCI-AEI-FEDER, UE).

REFERENCES

- Armus, L., Mazzarella, J. M., Evans, A. S., et al. 2009, PASP, 121, 559, doi: 10.1086/600092
- Battersby, C., Bally, J., & Svoboda, B. 2017, ApJ, 835, 263, doi: 10.3847/1538-4357/835/2/263
- Belloche, A. 2018, IAU Symposium, 332, 383, doi: 10.1017/S1743921317007815
- Belloche, A., Menten, K. M., Comito, C., et al. 2008, A&A, 482, 179, doi: 10.1051/0004-6361:20079203
- Belloche, A., Müller, H. S. P., Garrod, R. T., & Menten, K. M. 2016, A&A, 587, A91, doi: 10.1051/0004-6361/201527268
- Belloche, A., Müller, H. S. P., Menten, K. M., Schilke, P., & Comito, C. 2013, A&A, 559, A47, doi: 10.1051/0004-6361/201321096
- Beltrán, M. T., & de Wit, W. J. 2016, A&A Rv, 24, 6, doi: 10.1007/s00159-015-0089-z
- Bonfand, M., Belloche, A., Garrod, R. T., et al. 2019, A&A, 628, A27, doi: 10.1051/0004-6361/201935523
- Bonfand, M., Belloche, A., Menten, K. M., Garrod, R. T., & Müller, H. S. P. 2017, A&A, 604, A60, doi: 10.1051/0004-6361/201730648

- Budaiev, N., Ginsburg, A., Jeff, D., et al. 2024, ApJ, 961, 4, doi: 10.3847/1538-4357/ad0383
- Busch, L. A., Belloche, A., Garrod, R. T., Müller,
 H. S. P., & Menten, K. M. 2022, A&A, 665,
 A96, doi: 10.1051/0004-6361/202243383
- Caswell, J. L. 1996, MNRAS, 283, 606, doi: 10.1093/mnras/283.2.606
- Cesaroni, R. 2005, in Massive Star Birth: A Crossroads of Astrophysics, ed. R. Cesaroni, M. Felli, E. Churchwell, & M. Walmsley, Vol. 227, 59–69, doi: 10.1017/S1743921305004369
- Clark, P. C., Glover, S. C. O., Ragan, S. E., Shetty, R., & Klessen, R. S. 2013, ApJL, 768, L34, doi: 10.1088/2041-8205/768/2/L34
- Crockett, N. R., Bergin, E. A., Neill, J. L., et al. 2014, ApJ, 787, 112, doi: 10.1088/0004-637X/787/2/112
- Gao, Y., & Solomon, P. M. 2004, ApJ, 606, 271, doi: 10.1086/382999
- Garrod, R. T., & Herbst, E. 2006, A&A, 457, 927, doi: 10.1051/0004-6361:20065560
- Garrod, R. T., Jin, M., Matis, K. A., et al. 2022, ApJS, 259, 1, doi: 10.3847/1538-4365/ac3131

- Gieser, C., Beuther, H., Semenov, D., et al. 2021, A&A, 648, A66, doi: 10.1051/0004-6361/202039670
- Ginsburg, A., Glenn, J., Rosolowsky, E., et al. 2013, ApJS, 208, 14, doi: 10.1088/0067-0049/208/2/14
- Ginsburg, A., Parikh, M., Woillez, J., et al. 2016, Astroquery V0.3.1, v0.3.1, Zenodo, doi: 10.5281/zenodo.44961
- Ginsburg, A., Goddi, C., Kruijssen, J. M. D., et al. 2017, ApJ, 842, 92, doi: 10.3847/1538-4357/aa6bfa
- Ginsburg, A., Bally, J., Barnes, A., et al. 2018, ApJ, 853, 171, doi: 10.3847/1538-4357/aaa6d4
- Goddi, C., Ginsburg, A., Maud, L. T., Zhang, Q.,
 & Zapata, L. A. 2020, ApJ, 905, 25,
 doi: 10.3847/1538-4357/abc88e
- Goldsmith, P. F., & Langer, W. D. 1999, ApJ, 517, 209, doi: 10.1086/307195
- Henshaw, J. D., Barnes, A. T., Battersby, C.,
 et al. 2023, in Astronomical Society of the
 Pacific Conference Series, Vol. 534, Protostars
 and Planets VII, ed. S. Inutsuka, Y. Aikawa,
 T. Muto, K. Tomida, & M. Tamura, 83,
 doi: 10.48550/arXiv.2203.11223
- Henshaw, J. D., Longmore, S. N., Kruijssen,J. M. D., et al. 2016, MNRAS, 457, 2675,doi: 10.1093/mnras/stw121
- Herbst, E., & van Dishoeck, E. F. 2009, ARA&A, 47, 427,
 - doi: 10.1146/annurev-astro-082708-101654
- Hogg, D. W., Bovy, J., & Lang, D. 2010, arXiv e-prints, arXiv:1008.4686. https://arxiv.org/abs/1008.4686
- Houghton, S., & Whiteoak, J. B. 1995, MNRAS, 273, 1033, doi: 10.1093/mnras/273.4.1033
- Kauffmann, J., Bertoldi, F., Bourke, T. L., Evans, N. J., I., & Lee, C. W. 2008, A&A, 487, 993, doi: 10.1051/0004-6361:200809481
- Kruijssen, J. M. D., Dale, J. E., & Longmore,S. N. 2015, MNRAS, 447, 1059,doi: 10.1093/mnras/stu2526
- Kruijssen, J. M. D., & Longmore, S. N. 2013, MNRAS, 435, 2598, doi: 10.1093/mnras/stt1634
- Lada, C. J., Forbrich, J., Lombardi, M., & Alves,J. F. 2012, ApJ, 745, 190,doi: 10.1088/0004-637X/745/2/190
- Lis, D. C., & Carlstrom, J. E. 1994, ApJ, 424, 189, doi: 10.1086/173882

- Lis, D. C., & Goldsmith, P. F. 1990, ApJ, 356, 195, doi: 10.1086/168830
- Lu, X., Mills, E. A. C., Ginsburg, A., et al. 2019, ApJS, 244, 35, doi: 10.3847/1538-4365/ab4258
- Mangum, J. G., & Shirley, Y. L. 2015, PASP, 127, 266, doi: 10.1086/680323
- Markwick-Kemper, A. J., Remijan, A. J., & Fomalont, E. 2006, in American Astronomical Society Meeting Abstracts, Vol. 208, American Astronomical Society Meeting Abstracts #208, 51.01
- McGuire, B. A. 2018, ApJS, 239, 17, doi: 10.3847/1538-4365/aae5d2
- McMullin, J. P., Waters, B., Schiebel, D., Young, W., & Golap, K. 2007, in Astronomical Society of the Pacific Conference Series, Vol. 376, Astronomical Data Analysis Software and Systems XVI, ed. R. A. Shaw, F. Hill, & D. J. Bell, 127
- Mehringer, D. M., Goss, W. M., & Palmer, P. 1994, ApJ, 434, 237, doi: 10.1086/174721
- Meng, F., Sánchez-Monge, Á., Schilke, P., et al. 2019, A&A, 630, A73, doi: 10.1051/0004-6361/201935920
- —. 2022, A&A, 666, A31, doi: 10.1051/0004-6361/202243674
- Meurer, G. R., Heckman, T. M., Leitherer, C., et al. 1995, AJ, 110, 2665, doi: 10.1086/117721
- Mills, E. A. C., Ginsburg, A., Immer, K., et al. 2018, ApJ, 868, 7, doi: 10.3847/1538-4357/aae581
- Motte, F., Bontemps, S., & Louvet, F. 2018, ARA&A, 56, 41, doi: 10.1146/annurev-astro-091916-055235
- Nomura, H., & Millar, T. J. 2004, A&A, 414, 409, doi: 10.1051/0004-6361:20031646
- Ossenkopf, V., & Henning, T. 1994, A&A, 291, 943
- Pickett, H., Poynter, R., Cohen, E., et al. 1998, Journal of Quantitative Spectroscopy and Radiative Transfer, 60, 883, doi: https: //doi.org/10.1016/S0022-4073(98)00091-0
- Ramachandran, V., Hamann, W. R., Hainich, R., et al. 2018, A&A, 615, A40, doi: 10.1051/0004-6361/201832816
- Requena-Torres, M. A., Martín-Pintado, J., Martín, S., & Morris, M. R. 2008, ApJ, 672, 352, doi: 10.1086/523627

Sánchez-Monge, Á., Schilke, P., Ginsburg, A., Cesaroni, R., & Schmiedeke, A. 2018, A&A, 609, A101, doi: 10.1051/0004-6361/201730425

Sánchez-Monge, Á., Schilke, P., Schmiedeke, A., et al. 2017, A&A, 604, A6, doi: 10.1051/0004-6361/201730426

Schmiedeke, A., Schilke, P., Möller, T., et al. 2016, A&A, 588, A143,

doi: 10.1051/0004-6361/201527311

Shimonishi, T., Izumi, N., Furuya, K., & Yasui, C. 2021, ApJ, 922, 206,

doi: 10.3847/1538-4357/ac289b

Sobolev, A. M., Cragg, D. M., & Godfrey, P. D. 1997, A&A, 324, 211

Taquet, V., Wirström, E. S., & Charnley, S. B. 2016, ApJ, 821, 46,

doi: 10.3847/0004-637X/821/1/46

van der Tak, F. F. S., van Dishoeck, E. F., Evans, Neal J., I., & Blake, G. A. 2000, ApJ, 537, 283, doi: 10.1086/309011

van der Walt, D. J., & Mfulwane, L. L. 2022, A&A, 657, A63,

doi: 10.1051/0004-6361/202141807

Zinnecker, H., & Yorke, H. W. 2007, ARA&A, 45, 481,

doi: 10.1146/annurev.astro.44.051905.092549

APPENDIX

A. INTEGRATED INTENSITY MAPS

In Figure 16, we show integrated intensity maps for each of the CH_3OH transitions that were incorporated into the rotational diagrams, as reported in Section 2.3. Figure 16.1 shows the transitions used for Sgr B2(S), and the following Figures 16.2 to 16.10 show DS1 through DS9. The complete figure set (10 images) is available in the online journal. Red contours show the 1 mm continuum for each hot core at 3, 6, 8, 12, and 32σ .

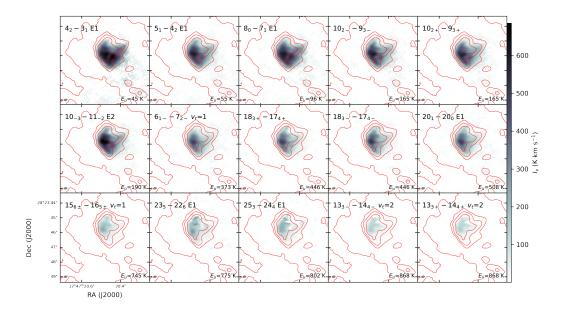


Figure 16. Integrated intensity maps of the detected CH_3OH emission lines in Sgr B2(S). E_u increases from left to right.

B. $N_{TRANSITION}$ MAPS

Figure 17 includes the $n_{transition}$ maps for the sources not shown in Figure 5. The maps are arranged with the left column showing sources DS2, DS4, DS6, and DS8, and the right column showing sources DS3, DS5, DS7, and DS9.

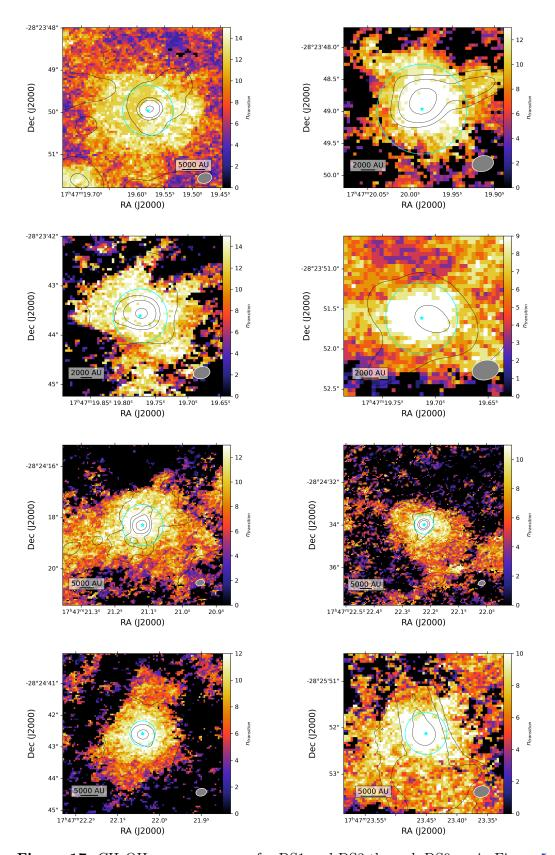


Figure 17. CH₃OH $n_{transition}$ maps for DS1 and DS3 through DS9, as in Figure 5.

C. ROTATIONAL TEMPERATURE MAPS

In Figure 18, we show the rotational temperature maps for each of the sources not discussed in Figure 6. The left column, from top to bottom, shows sources DS2, DS4, DS6, and DS8. The right column shows sources DS3, DS5, DS7, and DS9.

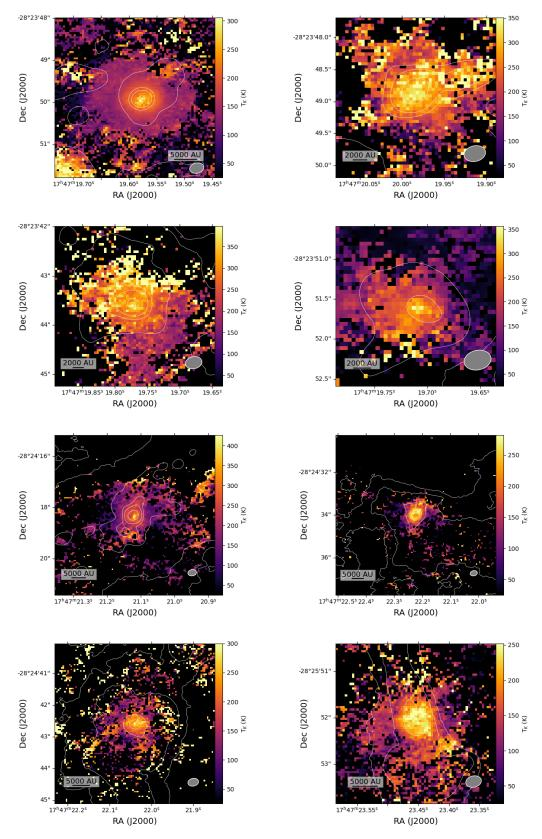


Figure 18. T_{rot} map for DS1 and DS3 through DS9, as in Figure 6. White contours show the 1 mm continuum at 3σ , 6σ , 8σ , 16σ , and 32σ levels ($\sigma = 0.2$ mJy beam⁻¹).

D. METHANOL LINE PANEL PLOTS

Figure 19 shows the CH₃OH lines used to make the temperature maps for the sources not discussed in Figure 4 (DS1-DS9), with each set of spectra pulled from the representative pixel of the source. The complete figure set (10 images) is available in the online journal.

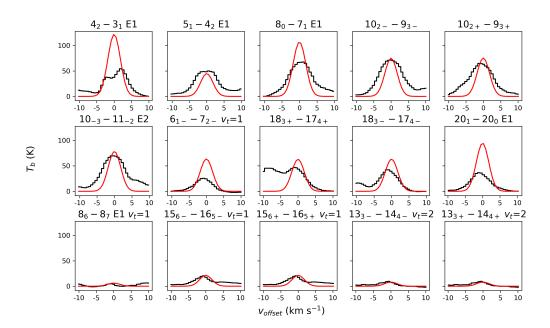


Figure 19. The same as Figure 4 for DS1.

E. SPECTRA

Figure 20 shows spectra from each source's representative pixel (see Table 2), as discussed in Section 3.1. The spectra are pulled from all four spectral windows in the data set and arranged in pairs, with spw0 and spw1 for a given core shown first and spw2 and spw3 shown in the following figure. The complete figure set (20 images, Figures 20.1-20.20) is available in the online journal.

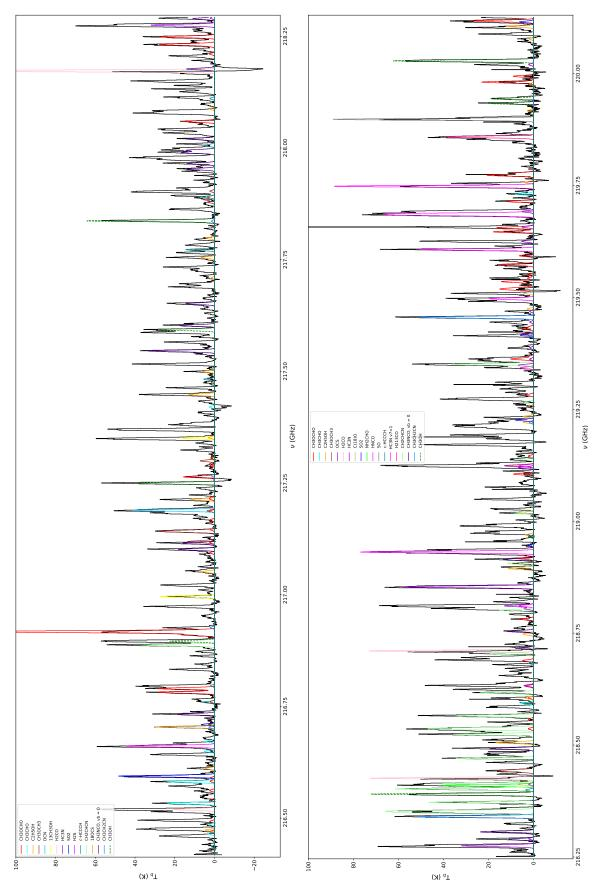


Figure 20. Spectra from the representative pixel of Sgr B2(S) showing the richness of its chemical composition. The black lines are the 1 mm ALMA spectral data. Colored lines are model spectra for CH₃OH and a selection of tentatively identified species created using the CH_3OH -derived T_{rot} measurement in the target pixel, by-eye estimates of N_{tot} , and the lte-molecule package of pyspeckit. CH_3OH lines are marked by the dashed green model lines.

F. RADIAL TEMPERATURE PROFILES

Figure 21 shows the radial temperature profiles for each source not discussed in Figure 7. The profiles are arranged in the same order as in Figure 17, with the left column showing sources DS2, DS4, DS6, and DS8, and the right column showing sources DS3, DS5, DS7, and DS9.

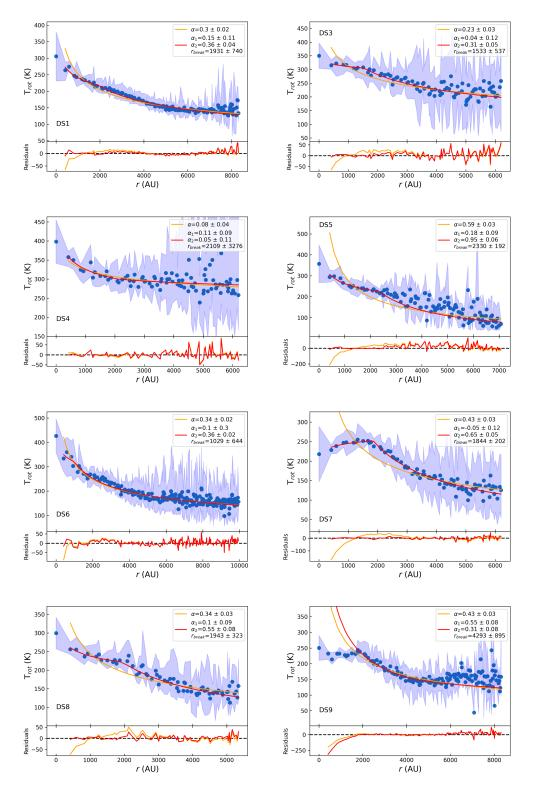


Figure 21. The same as Figure 7 but for DS1 and DS3 through DS9.

G. N_{H_2} MAPS

Figure 22 contains N_{H_2} maps for the hot cores in our sample, as discussed in Section 3.2.2. Contours show the 1 mm continuum for each hot core with levels at 3, 6, 8, 12, and 32σ .

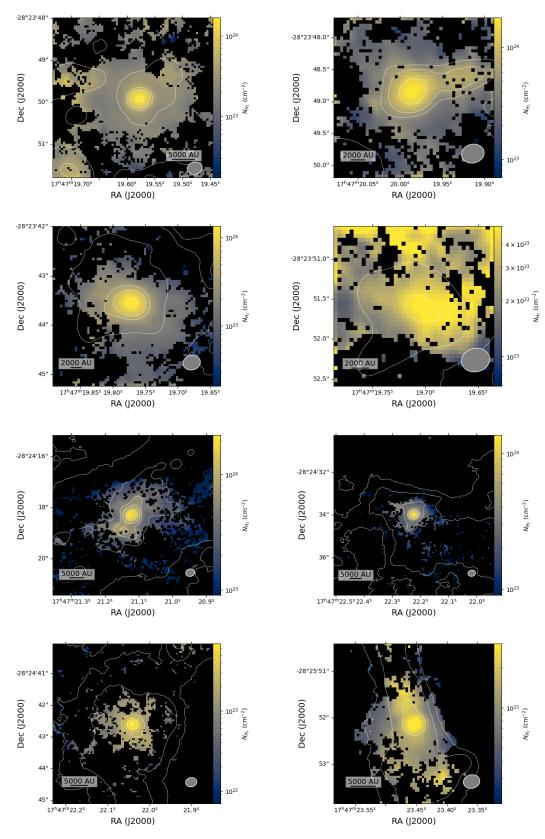


Figure 22. N_{H_2} maps for DS1 and DS3 through DS9. White contours show the 1 mm continuum at 3σ , 6σ , 8σ , 16σ , and 32σ levels ($\sigma = 0.2$ mJy beam⁻¹).

H. ABUNDANCE MAPS

Figure 23 contains X(CH₃OH) maps for the sources not shown in Figure 9. The maps are arranged in the same order as in Figure 22, with the left column showing sources DS2, DS4, DS6, and DS8, and the right column showing sources DS3, DS5, DS7, and DS9.

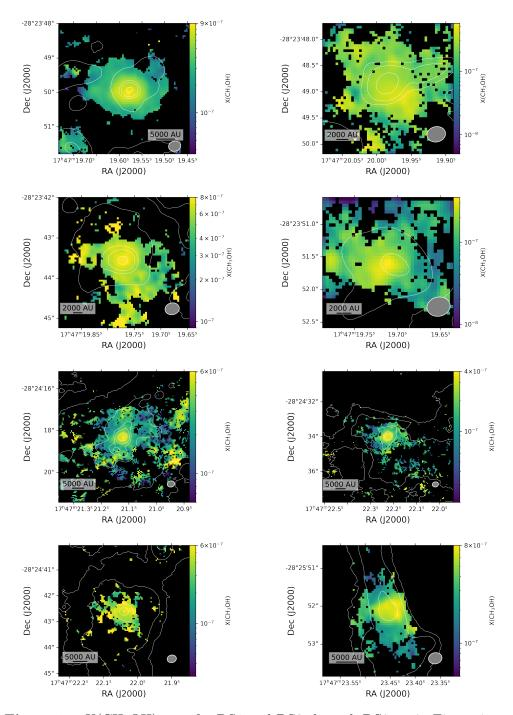


Figure 23. X(CH₃OH) map for DS1 and DS3 through DS9, as in Figure 9.

I. ABUNDANCE VERSUS TEMPERATURE DISTRIBUTIONS

Figure 24 includes the $X(CH_3OH)$ vs T_{rot} distributions for the sources not shown in Figure 10. The left column includes sources DS1, DS4, DS6, and DS8. The right column includes sources DS3, DS5, DS7, and DS9.

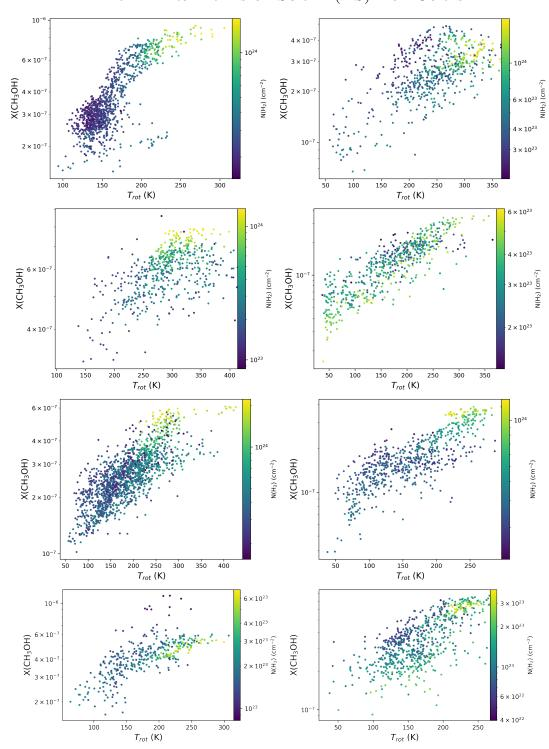


Figure 24. The same as Figure 10 for DS1 and DS3 through DS9.